AIMS Medical Science

AIMS Medical Science, 13(1): 33–49.
DOI: 10.3934/medsci.2026003
Received: 19 August 2025
Revised: 18 February 2026
Accepted: 02 March 2026
Published: 18 March 2026

http://www.aimspress.com/journal/medicalScience

Research article

Investigation on artery calcified plaque grinding mechanism

Haonan Xu[1], Yao Liu[1,*], Huaye Kong[1], Jinzhu Guo[1] and Bin Shen[2]

[1] Mechanical Engineering, North University of China, Taiyuan 030051, China
[2] Yangtze Delta Region Institute of Tsinghua University, Zhejiang, Jiaxing 314000, China

* **Correspondence:** Email: liuyao@nuc.edu.cn; Tel: 19834530812; Fax: +8603513925466.

Abstract: Plaque grinding is an interventional procedure for removing arterial obstructions using a high-speed rotational device on a flexible driveshaft. Complications have been reported in plaque grinding to limit population of the process. In order to reveal the calcified plaque grinding mechanism inside the artery, a series of experiments were conducted. The wheel motion was identified through high-speed camera observation and grinding marks identification. The effects of rotation speed, wheel diameter, and lumen size on the grinding force and debris size distribution were discussed. The findings demonstrated that the grinding wheel rotates along the guidewire and orbits around the lumen, exhibiting intermittent contact to remove plaque discretely. The complex wheel motion generates an irregular grinding force, which was identified through the implementation of statistical methods based on probability theory. It has been demonstrated that a decrease in wheel diameter and rotation speed and an increase in lumen size can result in a reduction in force. The debris size distribution was found to be primarily influenced by the wheel speed. The elevated wheel speed can result in smaller debris, owing to the reinforced impaction effect. This study provides a comprehensive understanding of the plaque grinding, which inform future clinical applications.

Keywords: calcified plaque; debris size; statistical method; grinding force; orbit

1. Introduction

Plaque is the accumulation of fat and calcium within arterial walls, specifically in the intima or media layer [1]. The shape of the plaque is extremely irregular with hardness comparable to human bone. Atherosclerosis develops through the deposition of LDL-C as fatty streaks, followed by

progressive accumulation of lipids, complex carbohydrates, hemorrhage, and thrombosis, which induces intimal fibrous hyperplasia and calcification, leading to plaque formation and expansion. With the aggravation of e disease, the media layer of the artery gradually degraded or even calcified. This process makes the artery wall gradually thicken and harden. With the calcified tissue continue to worsen, the vascular lumen becomes narrow or even completely blocked. The lumen size degradation limits blood flow and blood supply, which leads to cardiovascular disease. In one survey, about 20% patients undergoing percutaneous coronary intervention presented moderate or severe calcification plaques [2]. The high hardness of calcified plaque makes the delivery and expansion of angioplasty balloons and stents difficult. The stents may also exhibit inadequate expansion, insufficient expansion, and asymmetric expansion, which increase the risk of surgical complications [3–5]. Therefore, rotational atherectomy has emerged as a promising technique.

The plaque grinding process inserts a micro grinding wheel in the vascular lumen to remove blocked calcified plaque tissue, restore patency in blood vessels, and rebuild blood flow. The first calcified plaque grinding device, developed by Boston Scientific, is treated by welding an ellipsoid bur to rotate at speeds up to 240,000 rpm. In 1988, Bertrand et al. [6] performed the first coronary atherosclerotic plaque grinding with success. According to the US Cardiovascular Medicine Guidelines, plaque grinding is currently the only effective way to remove moderate and severe calcified plaque lesions from the artery [7]. Before grinding treatment, a special guidewire is used to pass through the distal end of the narrow lesion. The grinding wheel is pushed to the proximal end of the narrow lesion along the guidewire. Then, the grinding wheel rotates and pushes forward until it passes through the lesion. In the process of treatment, the size of the grinding wheel increases to expand the vascular lumen size. After rotary grinding, the plaque is ground into tiny particles, which enter the capillaries with the blood flow and are eventually absorbed by the liver, spleen, lungs, and endothelial phagocytes [8].

During the treatment, the rotational wheel produces a large grinding force, as well as a large amount of grinding debris. Those can cause various complications, including 16–67% of restenosis (the re-blockage of a vessel), due to vascular tissue damage caused by grit ablation [9–14]. The incidence of media and adventitia layer separation due to grinding force is 10–13% [9,11,12,15,16]. The incidence of slow flow/no-reflow (where capillaries are blocked by debris, preventing blood from returning to heart) ranges from 3 to 27%. [16–21]. Therefore, the study of plaque grinding mechanisms to reduce complications is of great significance in theory and reality.

However, studies on the calcified plaque grinding mechanism are limited. Shih's group [22]. built a multi-grit model using the smoothed particle hydrodynamics (SPH) method to study the grinding force in plaque grinding, they did a series of experiments to validate the grinding force oscillation patterns and their correlation with the wheel orbital motion, providing critical insights into the mechanics of the RA process. Zhu et al. [23] used simulation methods to study the rotational grinding process, which showed that the smaller the burr-to-artery-diameter ratio (B/A = 0.5) was, the more stable the flow field domain was. Additionally, the larger the diameter of the grinding wheel, the greater the pressure and stress it generates, which shows that the size of the grinding wheel has a significant impact on the stability of rotational atherectomy. Liu et al. [24] modeled the debris size distribution in plaque grinding, and the research elucidates the correlation between rotational speed and debris size. Adams et al. [25] used simulation to study the variation of centrifugal force with the lumen size during the orbit grinding and showed that the centrifugal force reached its maximum when the diameter of the blood vessel was about 4 mm. Zheng et al. [26] established a three-dimensional computational

fluid dynamics (CFD) model for the first time to simulate the orbital motion and flow field characteristics of the grinding wheel in RA. Simulation and experimental results show that high rotational speeds (e.g., 175,000 rpm) increase plaque removal efficiency but significantly increase grinding force. However, it did not specify the optimal rotational speed of the rotary grinding wheel without causing complications. Kohler et al. [27] used the finite element method to reveal that the grinding force increase as the rotational speed increase, which were verified using a carbon surrogate for calcified plaque grinding. Based on the aforementioned literature review, extensive research has been conducted on grinding forces during rotational atherectomy (RA), with well-established simulation and experimental methodologies. However, optimal strategies for grinding force optimization remain unexplored, and the quantitative impact of process parameters on grinding forces has not been systematically characterized. Given the critical role of grinding force modulation in enhancing RA safety, this study employs experimental investigations to elucidate the grinding mechanics and identify optimal force minimization strategies.

The purpose of this research is to study the plaque removal mechanism through the wheel motion, grinding force, and debris size distribution. The overall framework is as follows. To begin, the experimental setup and parameters are introduced. Then, the results of the wheel motion analysis are shown. Based on the motion result, the grinding force is extracted and analyzed by considering the grinding parameters effect. Next, the debris size distribution results are presented and discussed. Finally, the conclusions were given.

2. Experiment setup

2.1. Calcified plaque simulation materials

The graphite [27], bovine bone [28], and porcine aorta [29] have been used as the calcified plaque surrogate in previous studies, and some studies have pointed out that the composition of calcified plaques is similar to that of human bones [30–31]. In the existing studies on rotary grinding, the materials used as substitutes for calcified tissues vary greatly. There is still no substance that is universally recognized as the most suitable alternative for calcified plaques. The focus of this work is to simulate the basic mechanical interactions between the tool and hard calcified tissue during high-speed mechanical grinding, the bovine bone exhibits a typical Haversian system structure, and its density and mechanical properties are similar to calcified tissues. It can represent the key mechanical characteristics of calcified plaques, such as hardness, brittleness, and fracture behavior. Therefore, in this study, based on the tissue characteristics of calcified plaques, bovine bone was selected as a substitute for calcified plaques. It will be ground into a ring shape and placed in a PVC pipe, as shown in Figure 1.

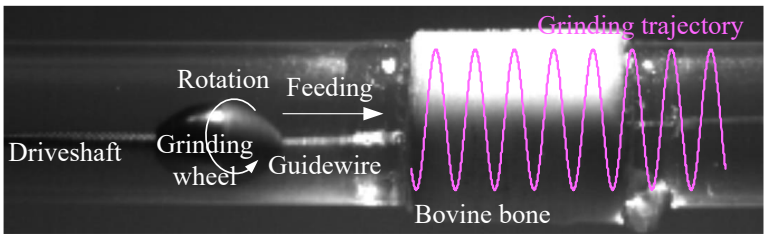

Figure 1. Grinding wheel motion setup.

2.2. Measurement of grinding wheel surface characteristics

Before the experiment, the grinding wheel surface was electroplated with abrasive grains. Due to the random spatial distribution of diamond abrasive grains on the grinding wheel surface, there are significant differences in their spatial orientation, protrusion height, and geometric morphology. The larger the size of the grinding wheel, the higher the cutting resistance it will generate. This is because the contact area between a single abrasive particle and the plaque is larger. In addition, grinding wheels with uneven height distribution of abrasive grains may be more prone to force fluctuations phenomena, as the protruding abrasive grains will bear greater impact loads. Therefore, measuring the surface characteristics of grinding wheels, such as the protrusion height and protrusion size of abrasive grains, plays an important role in analyzing the influence mechanism of grinding force.

The abrasive grains were observed using a confocal microscope, as shown in Figure 2(a). To obtain representative measurements, images were taken from 10 randomly selected positions on the wheel surface, and a total of 392 abrasive grains were measured. The procedures for measuring grain size and protrusion height are illustrated in Figure 2(a) and (b), respectively. The results, presented in Figure 2(c) and (d), indicate that the grain size ranged from 20 to 30 μm and the protrusion height ranged from 6 to 10 μm. These measurements provide a quantitative basis for understanding the role of grain topography in grinding performance and force behavior.

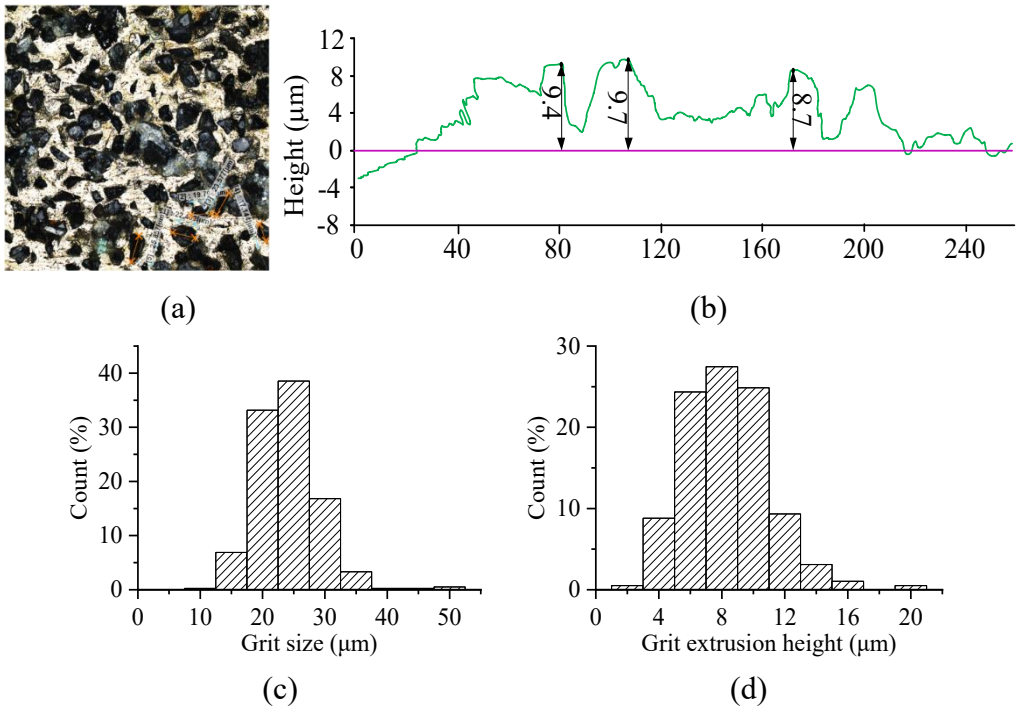

Figure 2. Grinding wheel. (a) Surface and grit size measurement, (b) extrusion height measurement, (c) grit size distribution, and (d) extrusion height distribution.

2.3. Rotary grinding test platform

Figure 3 gives the experiment setup in this study. The grinding device used in this study is from Boston Scientific, which consists of a gas supply tank, console, foot control panel, air turbine in a

handle unit, and catheter with an ellipsoidal grinding wheel. In this study, saline was employed as the cooling and lubricating fluid, serving as a transparent substitute for blood to facilitate clear visual observation and high-speed imaging of the tool motion and debris flow. While it is acknowledged that blood possesses higher viscosity and non-Newtonian properties compared to saline, the primary objective of this work is to investigate the fundamental mechanical interactions between the grinding wheel and calcified tissue, including grinding forces, debris generation, and wheel kinematics. The use of saline allows for the analysis of these key mechanical factors under controlled, repeatable conditions, minimizing the complexity introduced by biological fluids. Previous studies in rotational atherectomy simulation have commonly utilized saline or water-based fluids for similar mechanistic investigations [22–24,26]. Ring-shaped bovine bone with inner diameters of 4 mm and 6 mm was inserted into the PVC tube to simulate the plaque blockage, as shown in Figure 1. These diameters were selected as they represent a relevant range for moderately to severely calcified coronary segments often targeted by rotational atherectomy in clinical practice. The bone surrogate was rigidly fixed to a fixture mounted on the dynamometer (Kistler 9256C1 three-direction dynamometer) to measure the grinding force. The high-speed camera (Model FASTCAM-1024PCI, Photron) at a frequency of 18,000 frames per second was used to observe the grinding wheel position change with time.

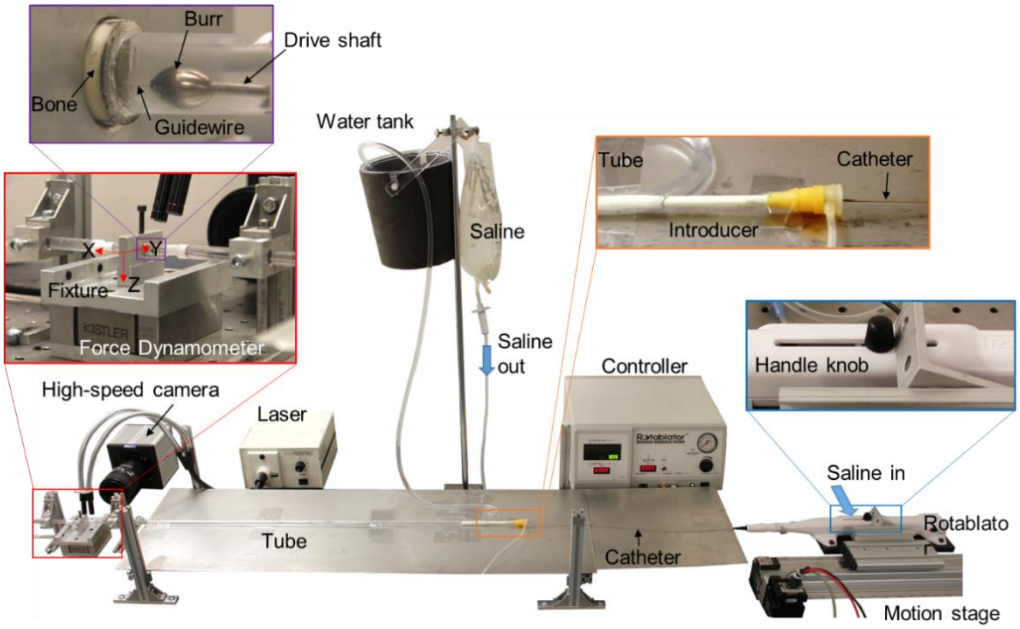

Figure 3. Experiment setup.

2.4. Experimental design of grinding wheel motion

To explore the movement trajectory of the grinding wheel, we designed the following experiment. First, the grinding wheel rotate outside the ring bone for motion capture. Then push the grinding wheel forward once through the ring bone for rotary grinding. Observe the grinding tracks to analyze the running trajectory of the grinding wheel. As the original surface profile of the ring-shaped bovine bone might affect the observation process, the inner surface of the ring-shaped bone was honed and polished before grinding. After the experiment, the ring bone was removed for cutting, and the scratches on the ground surface were observed by an environmental scanning electron microscope (ESEM).

2.5. Experimental design of grinding force and debris size

After the wheel motion was clarified, we conducted a series of experiments to explore the influence mechanism of different rotary grinding parameters on grinding force. The influence mechanism of parameters, such as the grinding wheel speed, the diameter of the vessel, and the diameter of the grinding wheel, on the grinding force is adjusted. The settings of each parameter are shown in Table 1.

The wheel diameter was chosen as 1.5 and 2.5 mm. Based on the lumen of human coronary and peripheral artery size, the 4mm and 6 mm inner diameter was selected in this study. The rotational speed used in clinical is recommended as 130,000–180,000 rpm [32], so the rotational speeds used in this study are 135,000, 145,000, 155,000, 165,000, and 175,000 rpm.

Table 1. Experiment parameters.

Experiments parameters	Values
Wheel diameter (mm)	1.5 and 2.5
Vessel diameter (mm)	4 and 6
Rotational speed (rpm)	135,000, 145,000, 155,000, 165,000, and 175,000

During the experiment, saline continuously flowed through the pvc pipe. The mixture of grinding debris and saline was collected to measure the particle size of the grinding debris. The size of the grinding debris was analyzed by the laser scattering method. Each testing was repeated five times for grinding force and debris size measurement.

3. Results and discussions

3.1. Grinding wheel motion

Figure 4 shows the front and left view grinding wheel images at different times. The picture was arranged based on the time. The brightest points on the front view of the grinding wheel and the wheel tip on the left view were chosen as the reference points for motion deduction. The reference points' locations were connected to show the wheel motion trajectory, which is a sine curve in both front and left view. The grinding wheel moves along the wall of the lumen, which shows the orbit motion, during the rotation process. The grinding wheel is close to the wall and the rotation can scratch on the wall to remove material. This combination of rotation and orbit motion makes the large lumen gain possible by using the single grinding wheel.

The orbit frequency was recorded by counting the orbit circles in the unit time through the images, as given in Figure 5. Under a 2.5 mm diameter grinding wheel in 4 mm lumen, the average orbit speed at 135,000, 145,000, 155,000, 165,000, and 175,000 rpm by five experiments is 6504, 6871, 7271, 7577, and 7893 rpm, respectively. The orbit frequency increases with the rotation speed, which means the high rotational speed can get the high material removal rate and efficiency. When the lumen diameter increases to 6 mm, the average orbit speeds decrease to 2676, 3017, 3428, 3785, and 4180 rpm, respectively. Compared to the 4 mm lumen, the orbit speed in 6 mm lumen decreased about 50%. The orbit frequency decreases as the lumen increases, which reduces the material removal rate and

efficiency. The correlation between the rotational speed and orbit speed was analyzed by the linear fitting, as given in Figure 5. According to the linear fitting results, the determination coefficient R^2 is calculated, which is up to 0.99. The orbital speed of the grinding wheel increases linearly with the rotational speed.

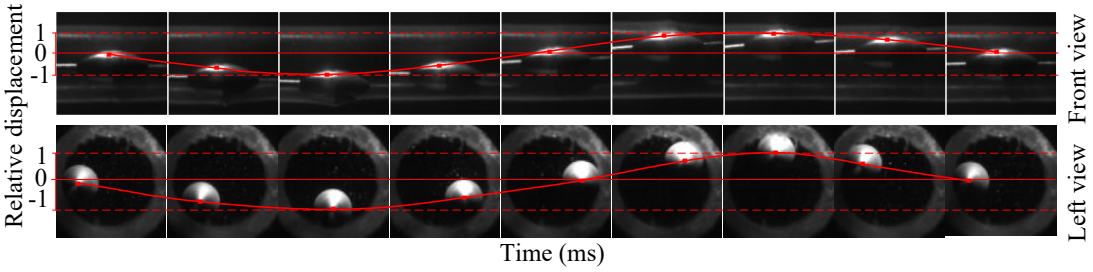

Figure 4. Grinding wheel location changing with time.

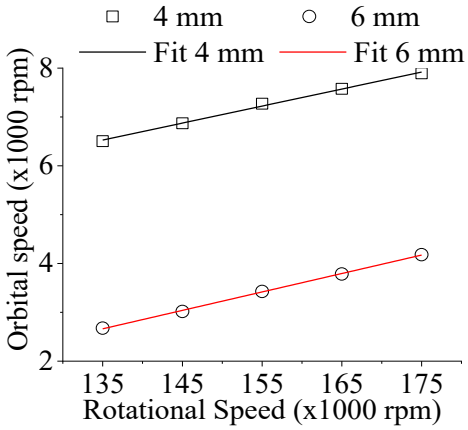

Figure 5. The orbit frequency of 2.5 mm wheel in 4 mm and 6 mm lumen.

3.2. Ground surface

Figure 6 gives the ground surface in single-pass experiments. Due to the limitation of the ESEM microscope's field of view, this measurement adopted image stitching after multiple measurements to obtain a larger measurement range and more measurement features, we rotated the emitter head of the ESEM to −60°, −30°, 0°, 30° and 60° respectively, and took five pictures from different positions. Then we manually assembled the five pictures. Then we manually assembled the five pictures. The composite image of the bone surface is shown in Figure 6(b). From the ESEM results, it can be seen that (1) the original surface after honing is very smooth, while after one grinding pass, discrete dark grinding marks appear on the surface and (2) these grinding marks are discontinuously distributed along the spiral trajectory formed by the combination of wheel revolution and axial feed motion, with significant variations in the distance between adjacent grinding points. The axial feed direction is indicated in Figure 6(b). Those discrete grinding marks indicate that there was also radial disengagement (Radial bouncing of the grinding wheel) of the grinding wheel during its rotational grinding process. The combination of the three movements of rotation, revolution and radial

disengagement ultimately left intermittent grinding marks on the bone surface. While our high-speed camera did not detect the radial bouncing displacement directly, this observation is consistent with the physical evidence from ESEM. The camera's spatial resolution was sufficient to track the orbital revolution but likely insufficient to capture small-amplitude radial motions that are nonetheless significant enough to cause intermittent contact, as unambiguously demonstrated by the discontinuous scratch pattern. Therefore, the ESEM evidence and the high-speed camera data are complementary.

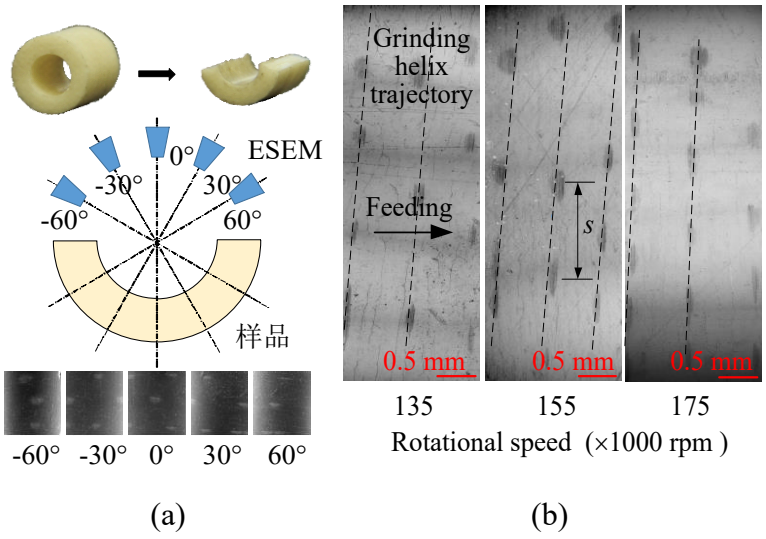

Figure 6. ESEM measurements grinding scratches. (a) Measurement process and (b) scratches on the ringbone surface.

By capturing the wheel location in the grinding process and checking the ground surface, the motion and material removal mechanism of the grinding wheel are clarified. The grinding wheel is driven by a driveshaft to rotate along its axis. This rotational motion induces a hydrodynamic effect that promotes orbital movement of the wheel along the lumen wall [26]. The combination of rotation and orbit motion enables the wheel to engage with and abrade the luminal surface. However, the normal force generated during abrasion causes the wheel to disengage radially from the wall. Thus, the wheel impacts and rebounds the wall continuously to leave some discrete markers on the ground surface. The radial disengagement of the grinding wheel leads to the impact force between the grinding wheel and the blood vessel wall, which may cause the dissection or even fracture of the blood vessels. The kinematic study of the grinding wheel clarified the movement and cutting law of the grinding wheel, which laid a foundation for the subsequent grinding force and debris size study, and guided the cardiovascular surgeon to understand the calcified plaque removal process and carry out the interventional treatment.

3.3. Grinding force

The motion of the grinding wheel during the rotary grinding process determined the grinding force. Based on the above motion analysis of the grinding wheel, the grinding force has not only the cutting force to remove the calcified plaque, but also the impaction force from radial disengagement of the grinding wheel, according to Newton's second and third law. Based on the wheel motion, the

grinding force can be divided into two stages. The first stage is the grinding wheel intermittently disengages from one contact point and re-engages at another. without coming into contact with the calcified tissue. During non-contact phases, the measured force reflects the energy required to sustain orbital motion. The second stage is when the grinding wheel collides with and cuts the calcified tissue. Figure 7 shows the original Y-axis grinding force F_G measured in ringbone (plaque surrogate) grinding experiments. The bone has an inner diameter of 4 mm and the rotation speed is 135,000 rpm. The force variation is very large with some peaks. Due to the rotational, orbital, and radial disengagement of the grinding wheel in the plaque grinding, the grinding force fluctuates greatly and exhibits significant periodicity. Besides, the large fluid hydrodynamics also cause the force variation. The huge variation makes the force determination very different.

In this study, a statistical method based on probability was proposed to get the actual grinding force for the plaque. Based on the force measure configuration, the maximum grinding force can only be captured when the grinding force direction is parallel to the dynamometer axis, which means the scratch occurred on the far left and right generatrix of an inner surface cylinder. Assuming the probability of measuring the grinding force in a revolution is P, the P can be calculated by the average total length of the scratches in one revolution divided by the circumference of the ringbone, which can be expressed as:

$$P = \sum l_i/\pi D \tag{1}$$

where D is the inside diameter of the ringbone and l_i is the length of i^{th} groove on the bone's inner surface in the one helix circle.

If the maximum grinding force cannot be measured in N revolutions is a small probability event in mathematics, which means the probability is less than 5%, then the revolutions N should meet the Equation (2).

$$1 - (1 - P)^N < 5\% \tag{2}$$

Based on the analysis above, the grinding force is the maximum force in N orbit revolution. Using the N revolution from the statistics method and orbit frequency, a window including the N revolution was added to the measured force. The maximum force in this window treated is the grinding force. The calculation process was shown in Figure 7.

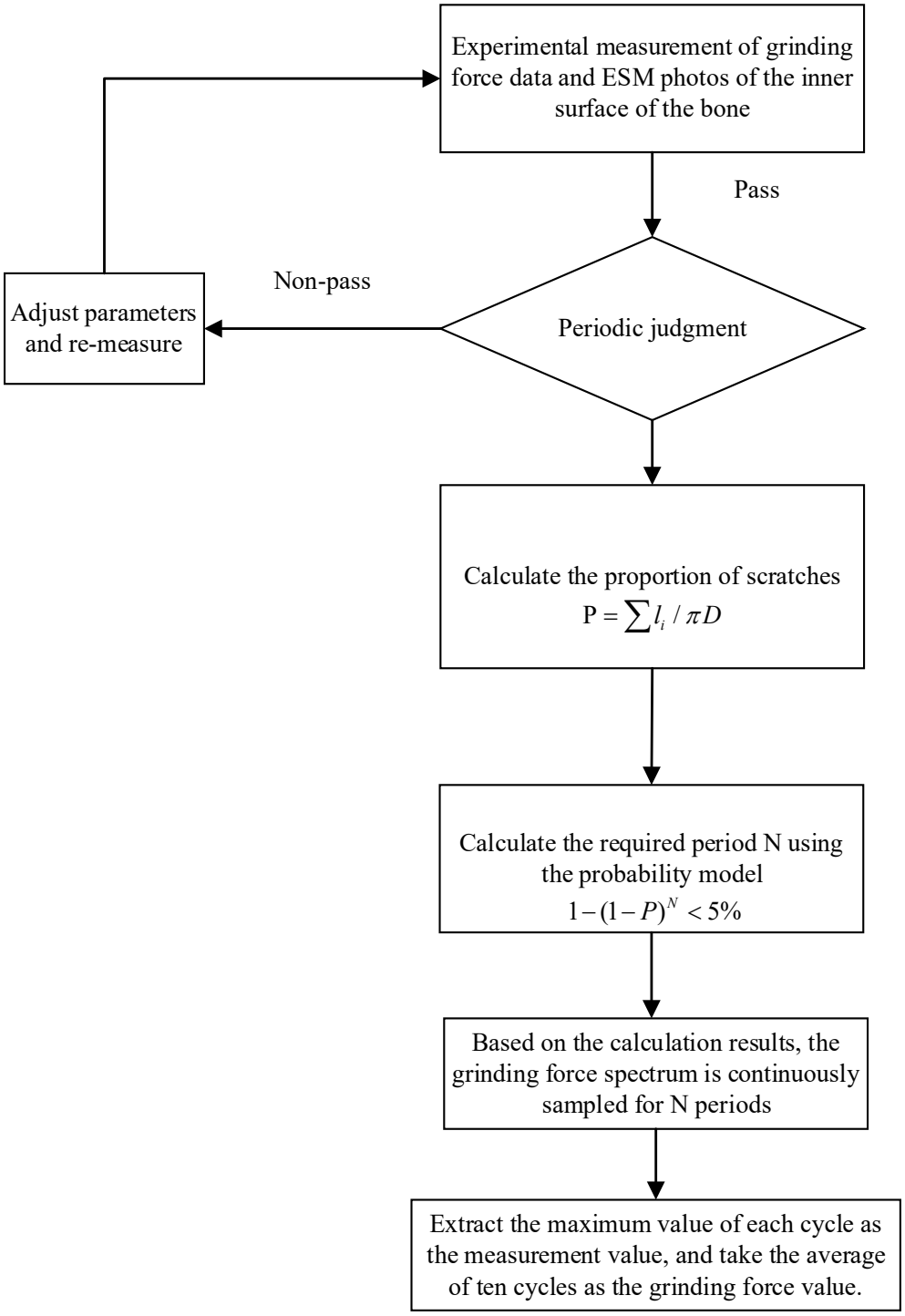

Figure 7. The grinding force calculation process based on probability statistical method.

Based on the ESEM results in Figure 6(b), the average scratch lengths were 0.368, 0.449, and 0.449 mm at 135,000, 155,000, and 175,000 rpm rotation speeds, respectively. The average distance between the scratches 1.04, 0.95, and 0.86 mm. The calculated P are 0.354, 0.472, and 0.522 of the inner circumferences of the ringbone, respectively. The calculated revolution N are 7, 5, and 5, respectively. Figure 8 gives the maximum grinding force in 7 revolutions, which is circled in red. Two grinding force points were circled, which are very similar. The average value of grinding force

measured per 10 revolutions is drawn in a black dotted line in Figure 8. The average grinding forces of five measurements at 135,000, 155,000, and 175,000 rpm were 1.84 ± 0.11(mean ± standard deviation, n = 5 independent experiments), 1.92 ± 0.04(n = 5), and 2.22 ± 0.01 N(n = 5), respectively. The standard deviation is only 6.0% of the force result, which indicates the reliability of the proposed statistics method.

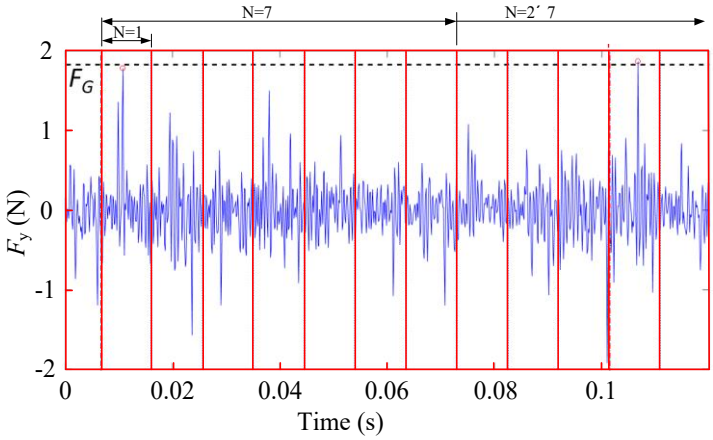

Figure 8. Force variation with time at a rotation speed of 135,000 rpm.

Figure 9 summarizes grinding force under different rotational speeds, wheel diameter, and lumen diameter. The grinding forces measured by the dynamometer, for the 2.5mm wheel in the 4 mm plaque surrogate lumen, at 135,000, 155,000, and 175,000 rpm rotational speeds are 1.84, 1.92, and 2.22N, respectively. The force increase caused by the wheel speed increase from 135000 to 175000 rpm is 20.6%. The force increase with the rotational speed trends are also found in 1.5 mm wheel-4 mm lumen and 2.5 mm wheel-6 mm lumen. Grinding force increased by 69.2% and 40% for the 1.5 mm wheel (4 mm lumen) and 2.5 mm wheel (6 mm lumen), respectively, as the rotational speed increased from 135,000 to 175,000 rpm, respectively.

As the wheel diameter decreases from 2.5 mm to 1.5 mm at 4 mm lumen, the grinding forces decrease to 0.13, 0.16, and 0.22 N at 135,000, 155,000, and 175,000 rpm rotational speed, respectively. Reducing wheel mass by 64% (calculated from diameter change) correlated with a more than 90% force reduction, suggesting mass dominantly influences impact forces. The grinding force can be effectively reduced by reducing the grinding wheel mass.

Compared to grinding 4 mm inner diameter bovine bone with a 2.5 mm diameter wheel, the grinding force of the 2.5 mm diameter grinding wheel in a 6 mm inner diameter was reduced by 0.53, 0.4, and 0.48 N, and the grinding force was reduced by 28%, 20%, and 20%. The grinding force on large-diameter blood vessels is smaller, so higher rotational speeds may be feasible in larger vessels to elevate the orbit speed, which can keep the safety and get high efficiency.

The grinding wheel impaction force is the main source of grinding force, accounting for more than 97% [33]. Controlling of the grinding force can be achieved by changing the grinding wheel acceleration and mass, according to Newton's second law. During the orbit motion of the grinding wheel, the linear speed remains the same. Therefore, the acceleration only causes the change of the velocity direction, which is correlated to the orbit speed. Based on this, the smaller lumen diameter and higher rotational speed can get the higher orbit speed. Compared to the results from 2.5–4 and

2.5–6 (*d*-*D*), an increase in blood vessel lumen can cause the wheel rotation speed to decrease, which reduces the wheel impact force. The above research and experimental results show that the use of a small-diameter grinding wheel or a grinding wheel with a small mass to grind calcified plaque can effectively reduce the grinding force, which is expected to eliminate vascular dissection and spasm caused by rotational ablation, reduce the damage to normal vascular tissue and the probability of re-stenosis, and ensure the efficient and safe development of rotational atherectomy interventional treatment. The present study was conducted in simulated vessels with inner diameters of 4 mm and 6 mm. It is acknowledged, however, that many diseased coronary arteries, particularly in distal segments or diffusely diseased vessels, can be narrower (<3 mm). In such narrower lumens, the confined space may alter the fluid dynamics and potentially amplify the interaction between the orbiting wheel and the vessel wall. But the fundamental mechanisms of motion (rotation, orbital revolution, and radial engagement) are expected to persist, the relative amplitude of radial bouncing could be measurably different.

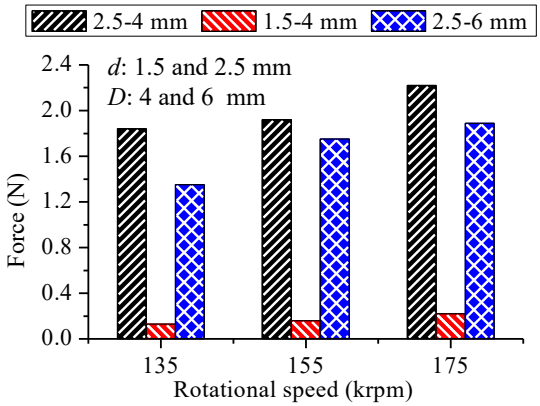

Figure 9. Grinding force under different wheel and vessel diameters.

3.4. Debris size distributions

Figure 10(a) gives the measured debris size distribution in the experiments. More than 90% of the debris size in the plaque grinding are between 0 and 30 μm, which indicates that the plaque grinding process can pulverize the plaque into small particles. Under the 2.5mm wheel diameter, with the increase of the rotational speed, debris size distribution curves become narrow and high in the small size range. For example, the maximum debris size volume percentage at 17,0000 rpm is 4 μm, which are 5 and 9 μm for 155,000 and 135,000 rpm, respectively. Figure 10(a) also gives the debris size distribution at a 1.5 mm diameter wheel and 230000 rpm, which has the debris size distribution between 155,000 and 135,000 rpm at 2.5 mm wheel diameter. The maximum debris size volume percentage is 6 μm. The results above indicate that the debris size distribution of plaque grinding is not only affected by the rotation speed of the grinding wheel, but also by the diameter of the grinding wheel.

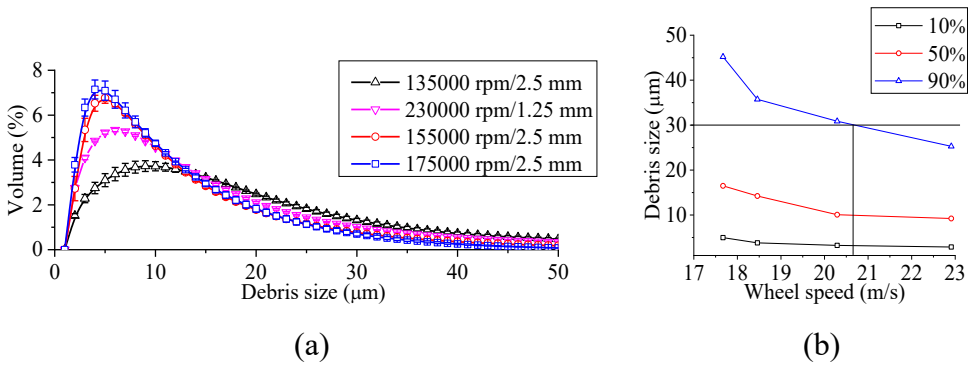

Figure 10. Debris size. (a) Distributions and (b) wheel speed effect.

Taking into account the rotational speed and wheel diameter comprehensively, the wheel speed from the grinding theory was used, which is defined as the linear speed at the wheel boundary. Figure 10(b) gives the effect of wheel speed on the debris size distribution. Three index values, which are the values that 10%, 50%, and 90% of the debris size in a volume less than, are chosen for the discussion. The index values are all decrease with the increase of the wheel speed. When the wheel speed is 17.7 m/s (2.5 mm grinding wheel at 135000 rpm), 90% of the debris is less than 45.19 μm. As the wheel speed increases to 22.9 m/s, 90% of the grinding debris is less than 25.29 μm.

This reduction in debris size can be attributed to a transition in material removal mechanism governed by impact energy and localized fracture behavior. At lower wheel speeds, the impact energy and force per unit time are relatively modest, often insufficient to induce complete fracture of the calcified tissue. Instead, material removal may occur through a combination of brittle micro-cracking and partial plastic deformation, leading to debris that remains partially connected or forms larger, irregular aggregates. As the wheel speed increases, the kinetic energy transferred during each impact rises proportionally to the square of the speed. This higher energy input promotes more complete fracture propagation within the material, facilitating a shift toward a more dominant brittle-fracture mode. Additionally, the increased strain rate at higher speeds enhances the likelihood of crack initiation and branching, resulting in finer debris. The large size of debris can block the capillary, which restricts the blood flow, resulting in the reduction of the blood return to the heart. Therefore, the debris size less than the blood cell was thought of as safe, which is defined as the 90% of debris size less than 30 μm in this study [24]. Based on the results in Figure 9(b), the wheel speed threshold is 20.7 m/s from the debris side. When calcified plaques are scribed into particles smaller than 30 μm, they can be absorbed by the blood cells and organs [22].

4. Conclusions

This study demonstrates the mechanism of plaque grinding. The main conclusions are as follows: (1) due to the radial disengagement of the grinding wheel during its movement, it is feasible to use a small-diameter grinding wheel to grind a large-diameter blood vessel; (2) The research results on grinding force confirm that the grinding force can be reduced by decreasing the rotational speed, using a small-diameter grinding wheel or a grinding wheel with a small mass, thereby effectively avoiding complications caused by excessive grinding force during rotational atherectomy; and (3) increasing the linear speed of the grinding wheel can effectively reduce the size of the grinding debris, thereby

improving and eliminating the slow blood flow/no-reflow caused by the blockage of capillaries by grinding debris during rotational atherectomy and enhancing the safety and reliability of the rotational atherectomy procedure. These findings advance the understanding for the plaque grinding process, and lays a foundation for further clinical study and application in the future.

Author contributions

The authors' contributions are as follows: Yao Liu was in charge of the whole experiments and manuscript preparation; Haonan Xu worked on experiments and manuscript preparation; Huaye Kong and Jinzhu Guo gave some guidance and manuscript proofreading. Bin Shen instructs the experiment design.

Use of AI tools declaration

The authors declare they have not used Artificial Intelligence (AI) tools in the creation of this article.

Acknowledgments

The authors sincerely thank Professor Albert Shih and Dr. Yihao Zheng at the University of Michigan for their help in the early experiment preparation. This research was supported by the Fundamental Research Program of Shanxi Province (CN) (Granted No. 202303021211146) and Opening Project of Guangdong Provincial Key Laboratory of Minimally Invasive Surgical Instruments and Manufacturing Technology (Granted No. MISIMT-2022-2).

Availability of data and materials

The datasets supporting the conclusions of this article are included within the article.

Conflict of interest

The authors declare no conflict of interest.

References

1. Mitsis A, Khattab E, Christodoulou E, et al. (2024) From cells to plaques: The molecular pathways of coronary artery calcification and disease. *J Clin Med* 13: 6352. https://doi.org/10.3390/jcm13216352
2. Lee MS, Yang T, Lasala J, et al. (2016) Impact of coronary artery calcification in percutaneous coronary intervention with paclitaxel-eluting stents: Two-year clinical outcomes of paclitaxel-eluting stents in patients from the ARRIVE program. *Catheter Cardiovasc Interv* 88: 891–897. https://doi.org/10.1002/ccd.26395
3. Takebayashi H, Kobayashi Y, Mintz GS, et al. (2005) Intravascular ultrasound assessment of lesions with target vessel failure after sirolimus-eluting stent implantation. *Am J Cardiol* 95: 498–502. https://doi.org/10.1016/j.amjcard.2004.10.020

4. Vavuranakis M, Toutouzas K, Stefanadis C, et al. (2001) Stent deployment in calcified lesions: Can we overcome calcific restraint with high-pressure balloon inflations?. *Catheter Cardiovasc Interv* 52: 164–172. https://doi.org/10.1002/1522-726X(200102)52:2<164::AID-CCD1041>3.0.CO;2-S
5. Virmani R, Farb A, Burke AP (1994) Coronary angioplasty from the perspective of atherosclerotic plaque: morphologic predictors of immediate success and restenosis. *Am J Cardiol* 127: 163–179. https://doi.org/10.1016/0002-8703(94)90522-3
6. Hansen DD, Auth DC, Vracko R, et al. (1988) Rotational atherectomy in atherosclerotic rabbit iliac arteries. *Am J Cardiol* 115: 160–165. https://doi.org/10.1016/0002-8703(88)90532-7
7. Levine GN, Bates ER, Blankenship JC, et al. (2011) 2011 ACCF/AHA/SCAI guideline for percutaneous coronary intervention: a report of the American College of Cardiology Foundation/American Heart Association Task Force on Practice Guidelines and the Society for Cardiovascular Angiography and Interventions. *J Am Coll Cardiol* 58: e44–e122. https://doi.org/10.1016/j.jacc.2011.08.007
8. Ahn SS, Auth D, Marcus DR, et al. (1988) Removal of focal atheromatous lesions by angioscopically guided high-speed rotary atherectomy: Preliminary experimental observations. *J Vasc Surg* 7: 292–300. https://doi.org/10.1016/0741-5214(88)90148-6
9. Kobayashi Y, Teirstein PS, Linnemeier TJ, et al. (2001) Rotational atherectomy (stentablation) in a lesion with stent underexpansion due to heavily calcified plaque. *Catheter Cardiovasc Interv* 52: 208–211. https://doi.org/10.1002/1522-726X(200102)52:2<208::AID-CCD1049>3.0.CO;2-H
10. Mittleider D, Russell E (2016) Peripheral atherectomy: applications and techniques. *Tech Vasc Interv Radiol* 19: 123–135. https://doi.org/10.1053/j.tvir.2016.04.005
11. Morii I, Miyazaki S (2000) Current overview of rotational atherectomy. does rotablator make sense. *Emodinamica* 22: 2–9. https://doi.org/10.1016/j.jcin.2013.12.196
12. Safian RD, Feldman T, Muller DW, et al. (2001) Coronary angioplasty and Rotablator atherectomy trial (CARAT): immediate and late results of a prospective multicenter randomized trial. *Catheter Cardiovasc Interv* 53: 213–220. https://doi.org/10.1002/ccd.1151
13. Tomey MI, Kini AS, Sharma SK (2014) Current status of rotational atherectomy. *JACC-Cardiovasc Interv* 7: 345–353. https://doi.org/10.1016/j.jcin.2013.12.196
14. Whitlow PL, Bass TA, Kipperman RM, et al. (2001) Results of the study to determine rotablator and transluminal angioplasty strategy (STRATAS). *Am J Cardiol* 87: 699–705. https://doi.org/10.1016/S0002-9149(00)01486-7
15. Dietz U, Rupprecht HJ, Ekinci O, et al. (2001) Angiographic analysis of immediate and long-term results of PTCR vs. PTCA in complex lesions (COBRA study). *Catheter Cardiovasc Interv* 53: 359–367. https://doi.org/10.1002/ccd.1181
16. Motwani JG, Raymond RE, Franco I, et al. (2000) Effectiveness of rotational atherectomy of right coronary artery ostial stenosis. *Am J Cardiol* 85: 563–567. https://doi.org/10.1016/S0002-9149(99)00812-7
17. Kini A, Reich D, Marmur JD, et al. (2001) Reduction in periprocedural enzyme elevation by abciximab after rotational atherectomy of type B2 lesions: results of the Rota ReoPro randomized trial. *Am Heart J* 142: 965–969. https://doi.org/10.1067/mhj.2001.119382

18. Matsuo H, Watanabe S, Watanabe T, et al. (2007) Prevention of no-reflow/slow-flow phenomenon during rotational atherectomy—a prospective randomized study comparing intracoronary continuous infusion of verapamil and nicorandil. *Am Heart J* 154: 994.e1–994.e6. https://doi.org/10.1016/j.ahj.2007.07.036
19. Sakakura K, Ako J, Wada H, et al. (2012) Comparison of frequency of complications with on-label versus off-label use of rotational atherectomy. *Am J Cardiol* 110: 498–501. https://doi.org/10.1016/j.amjcard.2012.04.021
20. Sharma SK, Dangas G, Mehran R, et al. (1997) Risk factors for the development of slow flow during rotational coronary atherectomy. *Am J Cardiol* 80: 219–222. https://doi.org/10.1016/s0002-9149(97)00325-1
21. Tsubokawa A, Ueda K, Sakamoto H, et al. (2002) Effect of intracoronary nicorandil administration on preventing no-reflow/slow flow phenomenon during rotational atherectomy. *Circ J* 66: 1119–1123. https://doi.org/10.1253/circj.66.1119
22. Shih AJ, Liu Y, Zheng Y (2016) Grinding wheel motion, force, temperature, and material removal in rotational atherectomy of calcified plaque. *CIRP Ann* 65: 345–348. https://doi.org/10.1016/j.cirp.2016.04.012
23. Zhu Z, Chen L, Yu W, et al. (2023) Numerical analysis of stress force on vessel walls in atherosclerotic plaque removal through coronary rotational atherectomy. *Micromachines* 14: 2148. https://doi.org/10.3390/mi14122148
24. Liu Y, Li B, Zheng Y, et al. (2017) Experiment and smooth particle hydrodynamics simulation of debris size in grinding of calcified plaque in atherectomy. *CIRP Ann* 66: 325–328. https://doi.org/10.1016/j.cirp.2017.04.090
25. Adams GL, Khanna PK, Staniloae CS, et al. (2011) Optimal techniques with the Diamondback 360 System achieve effective results for the treatment of peripheral arterial disease. *J Cardiovasc Transl Res* 4: 220–229. https://doi.org/10.1007/s12265-010-9255-x
26. Zheng Y, Liu Y, Pitre JJ, et al. (2018) Computational fluid dynamics modeling of the burr orbital motion in rotational atherectomy with particle image velocimetry validation. *Ann Biomed Eng* 46: 567–578. https://doi.org/10.1007/s10439-018-1984-z
27. Kohler R, Nguyen T, McBroom J (2014) Removal of calcified plaque utilizing orbital atherectomy. In: *International Manufacturing Science and Engineering Conference*, American Society of Mechanical Engineers. https://doi.org/10.1115/MSEC2014-4209
28. Reisman M, Shuman BJ, Harms V (1998) Analysis of heat generation during rotational atherectomy using different operational techniques. *Catheter Cardiovasc Diagn* 44: 453–455. https://doi.org/10.1002/(SICI)1097-0304(199808)44:4<453::AID-CCD21>3.0.CO;2-I
29. Gehani AA, Rees MR (1998) Can rotational atherectomy cause thermal tissue damage? A study of the potential heating and thermal tissue effects of a rotational atherectomy device. *Cardiovasc Interv Radiol* 21: 481–486. https://doi.org/10.1007/s002709900308
30. Alexopoulos N, Raggi P (2009) Calcification in atherosclerosis. *Nat Rev Cardiol* 6: 681–688. https://doi.org/10.1038/nrcardio.2009.165
31. Duer MJ, Friščić T, Proudfoot D, et al. (2008) Mineral surface in calcified plaque is like that of bone: further evidence for regulated mineralization. *Arterioscler Thromb Vasc Biol* 28: 2030–2034. https://doi.org/10.1161/ATVBAHA.108.172387
32. Barbato E, Carrié D, Dardas P, et al. (2015) European expert consensus on rotational atherectomy. *EuroIntervention* 11: 30–36. https://doi.org/10.4244/eijv11i1a6

33. Zheng Y, Liu Y, Liu Y, et al. (2019) Multigrain smoothed particle hydrodynamics and hertzian contact modeling of the grinding force in atherectomy. *J Manuf Sci Eng* 141: 041015. https://doi.org/10.1115/1.4042603